Open Archive Toulouse Archive Ouverte

OATAO is an open access repository that collects the work of Toulouse researchers and makes it freely available over the web where possible

This is an author's version published in: http://oatao.univ-toulouse.fr/24270

Official URL:

https://doi.org/10.1021/acs.inorgchem.9b00651

To cite this version:

Pinto, Juliano Schorne and Cassayre, Laurent and Presmanes, Lionel and Barnabé, Antoine *Insights on the Stability and Cationic Nonstoichiometry of CuFeO2 Delafossite.* (2019) Inorganic Chemistry, 58 (9). 6431-6444. ISSN 0020-1669

Any correspondence concerning this service should be sent to the repository administrator: tech-oatao@listes-diff.inp-toulouse.fr

Insights on the Stability and Cationic Nonstoichiometry of CuFeO$_2$ Delafossite

Juliano Schorne-Pinto,[†,‡] Laurent Cassayre,[†] Lionel Presmanes,[‡] and Antoine Barnabé[*,‡]

[†]Laboratoire de Génie Chimique, Université de Toulouse, CNRS, Toulouse, France

[‡]CIRIMAT, Université de Toulouse, CNRS, Université Paul Sabatier, 118 Route de Narbonne, 31062 Toulouse, Cedex 9, France

S *Supporting Information*
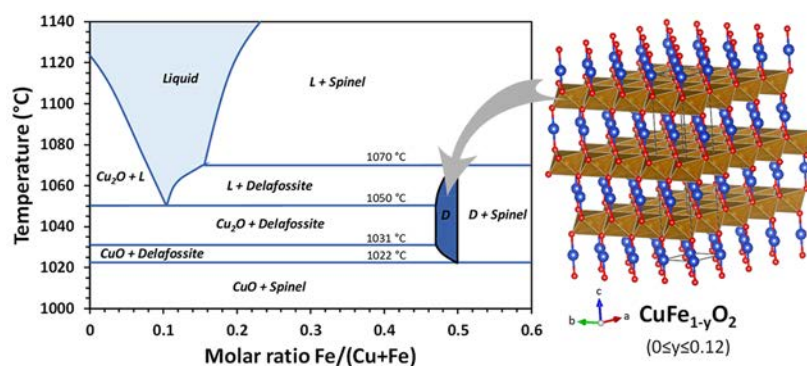
ABSTRACT: CuFeO$_2$, the structure prototype of the delafossite family, has received renewed interest in recent years. Thermodynamic modeling and several experimental Cu−Fe−O system investigations did not focus specifically on the possible nonstoichiometry of this compound, which is, nevertheless, a very important optimization factor for its physicochemical properties. In this work, through a complete set of analytical and thermostructural techniques from 50 to 1100 °C, a fine reinvestigation of some specific regions of the Cu−Fe−O phase diagram under air was carried out to clarify discrepancies concerning the delafossite CuFeO$_2$ stability region as well as the eutectic composition and temperature for the reaction L = CuFeO$_2$ + Cu$_2$O. Differential thermal analysis and Tammann's triangle method were used to measure the liquidus temperature at 1050 ± 2 °C with a eutectic composition at Fe/(Cu + Fe) = 0.105 mol %. The quantification of all of the present phases during heating and cooling using Rietveld refinement of the high-temperature X-ray diffraction patterns coupled with thermogravimetric and differential thermal analyses revealed the mechanism of formation of delafossite CuFeO$_2$ from stable CuO and spinel phases at 1022 ± 2 °C and its incongruent decomposition into liquid and spinel phases at 1070 ± 2 °C. For the first time, a cationic off-stoichiometry of cuprous ferrite CuFe$_{1−y}$O$_{2−δ}$ was unambiguous, as evidenced by two independent sets of experiments: (1) Electron probe microanalysis evidenced homogeneous micronic CuFe$_{1−y}$O$_{2−δ}$ areas with a maximum y value of 0.12 [i.e., Fe/(Cu + Fe) = 0.47] on Cu/Fe gradient generated by diffusion from a perfect spark plasma sintering pristine interface. Micro-Raman provided structural proof of the existence of the delafossite structure in these areas. (2) Standard Cu additions from the stoichiometric compound CuFeO$_2$ coupled with high-temperature X-ray diffraction corroborated the possibility of obtaining a pure Cu-excess delafossite phase with y = 0.12. No evidence of an Fe-rich delafossite was found, and complementary analysis under a neutral atmosphere shows narrow lattice parameter variation with an increase of Cu in the delafossite structure. The consistent new data set is summarized in an updated experimental Cu−Fe−O phase diagram. These results provide an improved understanding of the stability region and possible nonstoichiometry value of the CuFe$_{1−y}$O$_{2−δ}$ delafossite in the Cu−Fe−O phase diagram, enabling its optimization for specific applications.

1. INTRODUCTION

The present work focuses on the description of equilibrium phases of the Cu−Fe−O system, which has, for instance, a high technological interest in the copper (Cu) industry because iron (Fe) is a major contaminant of Cu scrap and ore.[1] In air, this system contains two mixed oxide phases, namely, cuprospinel and delafossite.

A large amount of research effort during the last decade has focused on the cuprospinel phase Cu$_z$Fe$_{3−z}$O$_4$, a well-known inverse spinel structure with cubic (space group $Fd\bar{3}m$) or tetragonal (space group $I4_1/amd$) symmetry depending on the temperature[2] and consisting of a solid solution between copper ferrite (z = 1, i.e., CuFe$_2$O$_4$) and magnetite (z = 0, i.e., Fe$_3$O$_4$). Fe-based spinels have been widely described in the literature because of their magnetic, electrical, and optical properties, with applications in catalysis[3−6] and battery electrodes[7,8] among others.[9−11]
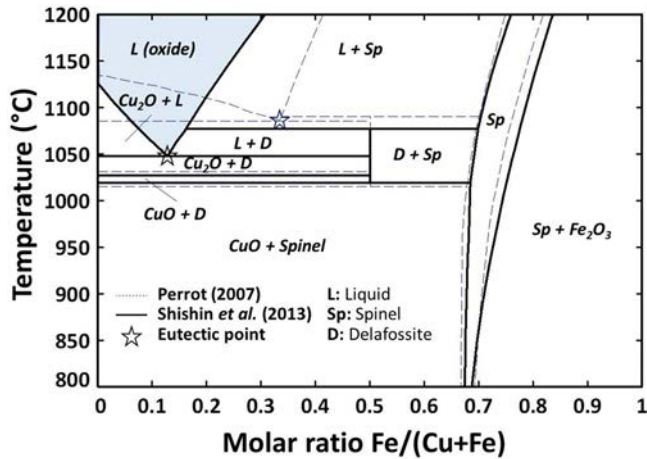
Figure 1. Phase diagrams of the Cu−Fe−O system in air, according to Perrot et al.[31] (dashed blue lines, drawn from the literature review) and Shishin et al.[33] (solid black lines, calculated from the thermodynamic model).

Conversely, the $CuFeO_2$ phase, which is the structure prototype of the delafossite family (first described by Friedel[12] in 1873 and named in honor of the French mineralogist and crystallographer Delafosse), did not attract much attention until the discovery of the properties of simultaneous transparency and p-type conductivity in this delafossite family.[13] $CuFeO_2$ has received renewed interest in recent years because of its photocatalytic properties for hydrogen production[14−19] as well as its photovoltaic[20] and/or thermo-electric[21−23] properties. This highly anisotropic phase crystallizes with the rhombohedral (space group $R\bar{3}m$) or hexagonal (space group $P6_3/mmc$) polytype. It is composed of compact

double layers of O atoms, with octahedral sites occupied by Fe^{3+} ions, and the cohesion between layers is ensured by Cu^+ ions in linear coordination.

1.1. Cu−Fe−O Phase Diagram in Air. Experimental investigations of the phase equilibria in the Cu−Fe−O system have been carried out for decades and led to the proposal of several phase diagrams.[1,24−30] Figure 1 (dashed blue lines) presents the phase diagram assessed by Perrot in 2007[31] based on an exhaustive literature analysis. Recently, two thermodynamic models of this system have been established with the CALPHAD (CALculations of PHase Diagrams) method, which is based on an assessment of the Gibbs energy functions for all phases of the system and allows the computation of phase diagrams. Khvan et al.[32] assessed the Cu−Fe−O system in 2011, and the model covers a temperature range between 650 and 1000 °C (not considered in this work). Shishin et al.[33] published another model in 2013 (solid black lines, Figure 1), which covers the high-temperature equilibria.

One can note that several areas of the diagram are consistent according to the different studies. First, the transition temperatures in the binary subsystems Cu−O and Fe−O are described similarly. Second, the stability region of the cuprospinel phase selected by Perrot et al. and based on the experimental results of Mexmain[34] and Kenfack and Langbein[35] is well represented by the thermodynamic model of Shishin et al.[33] Third, delafossite is always considered to be a stoichiometric compound $CuFeO_2$. However, there are also noticeable differences between the two diagrams plotted in Figure 1. The first is the stability range of the delafossite compound. Indeed, Perrot et al. selected a formation temperature of 1015 ± 2 °C and a decomposition temperature of 1090 ± 5 °C, based on the measurements done by Yamaguchi[25] in 1966. The same transition temperatures

Table 1. Published Values for the Lattice Parameters of Some Delafossite $CuFeO_2$ at Room Temperature

lattice constant							
a (Å)	c (Å)	c/a	V (Å³)	form	synthesis	year	ref
3.0351	17.156	5.65	136.87	single crystal	hydrothermal	1971	Shannon et al.[49,50]
3.030	17.15	5.66	136.36	single crystal	flux method	1988	Dordor et al.[51]
3.032	17.15	5.66	136.54	single crystal	flux method	1988	
3.037	17.19	5.66	137.31	single crystal	flux method	1993	Mekata et al.[52]
3.036	17.169	5.66	137.05	single crystal	floating zone	1995	Zhao et al.[53]
3.033	17.136	5.65	136.52	single crystal	flux method	2009	Omeiri et al.[54]
3.03(3)	**17.16(2)**	**5.66(1)**	**136.8(4)**	**single crystal**	**average**		
3.03	17.09	5.64	135.88	powder	solid-state reaction	1967	Muir et al.[55]
3.032	17.153	5.66	136.56	powder	solid-state reaction	1987	Doumerc et al.[56]
3.035	17.16	5.65	136.89	powder	solid-state reaction	1988	Dordor et al.[51]
3.041	17.21	5.66	137.83	powder	solid-state reaction	1993	Mekata et al.[52]
3.03	17.144	5.66	136.31	powder	solid-state reaction	1997	Zhao et al.[57]
3.03333	17.1582	5.66	136.72	powder	solid-state reaction	2000	Sukeshini et al.[58]
3.0345	17.166	5.66	136.89	powder	solid-state reaction	2003	El Ataoui et al.[59]
3.0351	17.1691	5.66	136.97	powder	solid-state reaction	2006	Mugnier et al.[45]
3.035	17.162	5.65	136.90	powder	hydrothermal	2006	Sheets et al.[60]
3.0344	17.158	5.65	136.82	powder	solid-state reaction	2009	Lalanne et al.[61]
3.03	17.14	5.66	136.28	powder	solid-state reaction	2010	Pavunny et al.[62]
3.0334	17.1598	5.66	136.74	powder	solid-state reaction	2011	Ruttanapun et al.[63]
3.035	17.16	5.65	136.89	powder	solid-state reaction	2013	Amrute et al.[64]
3.038	17.167	5.65	137.27	powder	mineral	2013	Kucerova et al.[65]
3.037	17.168	5.65	137.13	powder	hydrothermal	2016	Sarabia et al.[66]
3.03	17 14	5.66	136.28	powder	solid-state reaction	2017	Rudradawong al.[23]
3.034(3)	**17.16(2)**	**5.66(1)**	**136.8(5)**	**powder**	**average**		

calculated by the model of Shishin et al.[33] are 1019 and 1077 °C, respectively. The second flagrant inconsistency for this system is the composition and temperature of the eutectic L = $CuFeO_2$ + Cu_2O in air, highlighted by a star symbol in Figure 1. Yamaguchi[25] suggested a eutectic temperature at 1080 °C, while the one announced by Buist et al.[24] is lower than 1036 °C. The eutectic temperature obtained from the thermodynamic model is 1049 °C. Similarly, the composition of the eutectic is not unanimously defined and ranges from 0.13 to 0.33 (based on the Fe molar ratio). It is particularly difficult to select one or the other coordinates because of their limited number and the variability of available experimental data.

1.2. Delafossite $CuFeO_2$ Stoichiometry. The exact composition of the delafossite compound has been controversial for a long time. In the early 1900s, Rogers[36] determined the formula $CuFeO_2$ ($Cu_2O \cdot Fe_2O_3$) after leaching in sulfuric acid and chemical analysis. In the 1960s, Buist et al.[24] proposed a new formula ($Cu_6Fe_3O_7$), deduced from weight loss on thermal analysis. Three years later, a new investigation was performed by Wiedersich et al.[37] coupling X-ray diffraction (XRD), Mössbauer spectroscopy, and chemical analytical techniques. The $Cu_6Fe_3O_7$ ($3Cu_2O \cdot Fe_3O_4$) compound could not be stabilized and was thus ruled out. $CuFeO_2$ was finally established as the only composition for delafossite. Hey[38] confirmed this result using natural delafossite, and Schaefer et al.[26] provided more data under low O_2 pressure (1×10^{-4}–5×10^{-1} atm) in the 900–977 °C temperature range. Because of the lack of accuracy of the analytical devices available for these early studies, small deviations in the cationic stoichiometry of the delafossite phase were not truly investigated.

In the past decade, small deviations of the cationic stoichiometry have been evidenced in a few compounds of the delafossite family, such as $Cu_{1-y}GaO_2$ ($-0.01 \leq y \leq 0.02$),[39] $Cu_{1+y}Mn_{1-y}O_2$ ($0 \leq y \leq 0.2$),[40] and $CuCr_{1-y}O_2$ ($0 \leq y \leq 0.1$).[41] To a larger extent, this can even considerably improve the properties of certain materials such as, for example, the p-type transparent conducting $Cu_{1-y}Cr_{1+y}O_2$ thin film.[42] Significant quantities of O (δ) can also be intercalated into the Cu planes of the $CuMO_2$ delafossite structure according to $CuMO_{2+\delta}$. This requires a cation M^{3+} exceeding a certain size and leads to an off-stoichiometric value δ, which can reach 0.66 when $M^{3+} = La^{3+}$, corresponding to a Cu^+/Cu^{2+} (and even Cu^{2+}/Cu^{3+}) mixed valence.[43,44] To date, because of the relatively small size of the Fe^{3+} cation, only limited O nonstoichiometry ($0.08 \leq \delta \leq 0.18$) has been reported on $CuFeO_{2+\delta}$ delafossite-type powders[23,45] or single crystals.[46,47] No work has so far provided real evidence of the existence of a cationic nonstoichiometry in $CuFeO_2$, but some indications available in the literature, however, suggest this eventuality. Indeed, in a recent work, Wuttig et al.[14] reported Cu nonstoichiometry in $Cu_{1-y}FeO_2$, with y values as low as 0.005 and 0.02, but they did not provide elemental or structural proof of the existence of the delafossite structure. Furthermore, in a recent chemical measurement of an inclusion phase in a Cu matrix,[48] the chemical formula $CuFe_{0.87}O_{1.79}$ was proposed. Once again, no structural analysis was provided to confirm the existence of this Cu-rich delafossite.

To complete this review on the $CuFeO_2$ delafossite phase stoichiometry, an exhaustive list of the available crystallographic data is reported in Table 1 for powders and single-crystal samples. Thin-film materials were intentionally excluded because of the potential stress and strain induced by the growing method and substrate nature. Despite the various synthesis conditions, the accuracy of the measurement techniques, and the possible O off-stoichiometry, remarkably grouped values are obtained for these lattice parameters. Whatever the single-crystal or powder samples, the standard deviation of the lattice constants is very narrow, i.e., 1.3% along the [100] direction, 3.5% along [001], and 0.6% in volume. Because there is no significant difference between all of the reported lattice constants, it is hard to suspect a cationic nonstoichiometry, and up to now, the cationic molar ratio Fe/(Cu + Fe) has always been considered to be equal to 0.5 in the delafossite phase.

1.3. Research Questions. According to our bibliographic review, it appears that several important elements are missing to describe accurately the Cu−Fe−O system in air. The first concern is the stability region and phase boundaries of the delafossite phase, which are substantially different in the various available phase diagrams and models and need to be revisited. The second is related to the eutectic composition and temperature for the equilibrium L = $CuFeO_2$ + Cu_2O. Finally, the possibility of a degree of cationic nonstoichiometry in delafossite needs to be closely investigated.

In the present work, we address these open questions through the implementation of an experimental study combining in situ high-temperature XRD (HT-XRD), thermal analysis, and accurate compositional analysis on various oxide mixtures. Precise monitoring of the delafossite composition range was also realized through a diffusion couple between copper and iron oxides.

Such a better description of the Cu−Fe−O phase diagram is crucial because it will permit one not only both to minimize the experimental effort and to improve the general understanding of the processes for producing these phases with the delafossite structure,[60,61,67−69] but also to optimize the remarkable properties of $CuFeO_2$ by a better understanding of the complex relationships between the structure and properties.[13−23,70]

One can note that, because some major applications of $CuFeO_2$ materials concern the surface properties, it also should be interesting to consider similar analysis on film. Even if thin-film materials could be characterized by an ad-hoc method, the equilibrium conditions are generally not satisfied because of, for instance, an almost instantaneous transition of the elements of the very high-temperature plasma to a crystalline solid phase at low temperature in the physical vapor deposition process. It is, however, possible to establish experimental "metastable" phase diagrams, representing the nature of the phases formed depending on the composition of the system and the deposition conditions of the thin films.[71] In recent work, Schneider et al.[72] developed a predictive approach to calculating metastable phase diagrams according to the power applied, based on the determination, by ab initio calculations, of the surface diffusion properties of the element constituents of the system. These calculations strongly rely on the most accurate description of the system at equilibrium, such as that presented in the present work for the Cu−Fe−O phase diagram.

2. EXPERIMENTAL SECTION

2.1. Materials. *Oxide Powder Precursors.* Two different batches of $CuO-Fe_2O_3$ powders were used: (i) CuO (Acros Organics; >99%), α-Fe_2O_3 (Alfa Aesar; 99.5%), and Cu_2O (Alfa Aesar; 99%) for

Table 2. Samples Compositions Measured by Weighing, XRF, and ICP-AES

precursor (wt %)		x = Fe/(Cu + Fe)		
CuO	Fe$_2$O$_3$	weighing	XRF	ICP-AES
100	0	0	0.00	0.00
75.04	24.96	0.25	0.27(1)	0.25(1)
59.98	40.02	0.40	0.40(1)	0.38(1)
49.91	50.09	0.50	0.50(1)	0.48(1)
40.01	59.99	0.61	0.59(1)	0.61(1)
24.92	75.08	0.75	0.73(1)	0.73(1)
0	100	1.00	1.00	1.00

Table 3. Rietveld Refinement Correction Parameters

precursor	Z	I/I_c	ref	$(\mu/r)^a$ (cm^2/g)
CuO	37	4.98	PDF 80-0076	42.21
Cu$_2$O	66	8.28	PDF 77-0199	45.70
CuFeO$_2$	71	2.09	PDF 39-0246	133.96
Fe$_2$O$_3$	76	2.40	PDF 33-0664	213.06
CuFe$_2$O$_4$	113	5.13	PDF 73-2315	156.25

^{a}Mass absorption coefficients were determined at 8.05 keV $[\lambda(K\alpha)]$ using physics.nist.gov/PhysRefData/FFast/html/form.html.

XRD investigations; (ii) CuO (Alfa Aesar; 99.998%) and α-Fe$_2$O$_3$ (Alfa Aesar, 99.995%) for thermal analysis. All samples were prepared by weighing the starting binary oxides in the desired proportions and mixing them in an agate mortar until a homogeneous mixture was obtained. The nominal composition of five mixed samples is presented in Table 2. The cationic molar ratio of the samples was controlled by X-ray fluorescence (XRF; S2 Ranger, Bruker) and inductively coupled plasma-atomic emission spectroscopy (ICP-AES; Ultima 2, Jobin Yvon) after dissolution in aqua regia. The three techniques provide very similar compositional values for all samples in the limit of their accuracies. In the following, all samples are identified by their nominal compositions in the scale of molar fractions x = Fe/(Cu + Fe), with the ratio obtained from the weighing data, which are accurate enough to evaluate this ratio x with two decimals.

Delafossite CuFeO$_2$ Powder. A polycrystalline sample of CuFeO$_2$ was prepared by a standard solid-state reaction according to a process described in a previous work:[61] Cu$_2$O and Fe$_2$O$_3$ powders of batch (i) were mixed in stoichiometric quantities and then treated in a nitrogen atmosphere between 900 and 1000 °C for 30 h with intermittent grinding.

Diffusion Couple. A spark plasma sintering (Fuji 632 Lx) device was used to prepare a bilayer sample, where each layer corresponds to one of the binary oxides of batch (i). The following conditions were applied: pressure of 50 MPa; C mold under an argon atmosphere; heating rate of 100 °C/min, dwell time of 7 min at 750 °C; cooling rate of 150 °C/min. After a dense bilayer sample (96% of theoretical maximum value) was obtained, the bulk was cut and annealed in a muffle furnace (Nabertherm) under an air atmosphere at 1045 °C for 30 min (heating rate of 5 °C/min; cooling rate of 10 °C/min).

2.2. Characterization Methods. *Composition Analysis.* The stoichiometries of copper−iron mixed oxides formed in the diffusion couple experiment were measured by field-emission-gun electron probe microanalysis (EPMA; SX Five FE, CAMECA).

Microstructural Analysis. The distribution sizes of the CuO and Fe$_2$O$_3$ precursors were determined using a laser diffraction particle size analyzer (Malvern Instruments, Mastersizer 3000) with an Aero S dry powder dispersion attachment. Control of the diffusion couple interface was carried out by field-emission-gun scanning electron microscopy (SEM) using a Jeol JSM 7800F microscope.

Thermal Analysis. Thermogravimetric analysis (TGA) and differential thermal analysis (DTA) were carried out using a Seteram TGA/DTA 92 instrument in flowing air, in order to measure the transition temperatures. Samples of around 20 mg placed in alumina crucibles

were heated from 25 to 1100 °C, at heating and cooling rates of 5 °C/min. Different rates of 1 and 10 °C/min to heating and cooling, respectively, were also applied to resolve some close transitions. Gold (T_{melting} = 1064.18 °C) was used as the reference material to calibrate the setup around the working temperature. The resulting accuracy for temperatures is ±2 °C.

Structural Analysis. In order to perform local structural characterization at room temperature in the diffusion couple samples, micro-Raman spectroscopy was carried out using a Jobin Yvon-Horiba LabRam Infinity spectrometer (from 100 to 1000 cm^{-1} with a 532 nm laser). For global structural analysis, HT-XRD measurements were performed using a Bruker D8 diffractometer $[\lambda(\text{Cu K}\alpha_1)$ = 1.54056 Å and $\lambda(\text{Cu K}\alpha_2)$ = 1.54443 Å radiation; nickel filter] equipped with an Anton Parr HTK1200N high-temperature chamber under an air, a nitrogen, or a primary vacuum atmosphere. A Bruker LynxEye detector was used in a 1D mode for rapid acquisition. The HT-XRD patterns were collected from 50 to 1100 °C, under isothermal conditions in steps of 50 °C, and with a heating rate of 30 °C/min between dwells. The acquisition conditions were 2θ within 15−75°, with a step size of 0.02° and a counting time of 1.11 s. Crucibles in alumina were used. Some tests have also been done in a ZrO$_2$ crucible to confirm that no problem with aluminum diffusion (which can form the parent compound CuAlO$_2$ in a Cu-rich region) occurs with the Al$_2$O$_3$ crucibles. A second set of measurements was made from 975 to 1045 °C, under isothermal conditions in steps of 5 °C and a heating rate of 30 °C/min between dwells. The conditions were 2θ within 17−69°, with a step size of 0.02° and a counting time of 1.85 s. The total acquisition duration was 80 min per diffraction pattern.

Phase identification was performed with the *DiffracPlus EVA* software combined with the PDF database and subsequently refined by the Rietveld method using the *Full Prof-Win Plot* program.[73,74] The Rietveld refinement method was used to determine the lattice constants as well as quantify the amount of crystalline phases at each temperature. The lattice constant standard deviations were systematically balanced by the quality of the refinement. In order to obtain an accurate quantification whatever the mass fraction of the constituent phases, i.e., to be in agreement with the pristine values reported in Table 2, intensity corrections had to be applied in the Rietveld refinement. First, an internal standard correction was applied using the reference intensity ratio (RIR) from the sample to corundum (I/I_c) obtained in the PDF database. Second, differential microabsorption between phases was taken into account by applying the Brindley correction method.[75,76] The Brindley intensity correction factor $\tau_{i,m}$ of phase i in mixture m is defined by eq 1:

$$\tau_{i,m} = \frac{1}{V_i} \int_O^{V_i} e^{-(\mu_i - \mu_m)^x} \, dV_i \tag{1}$$

where V_i, μ_i, and ρ_i are the volume, linear absorption coefficient, and density of phase i, respectively. The average linear absorption coefficient of the mixture μ_m is defined by eq 2:

$$\mu_m = \rho_m \sum w_i \frac{\mu_i}{\rho_i} \tag{2}$$

where ρ_m is the density of the mixture m and w_i the mass fraction of phase i.

The expression of $\tau_{i,m}$ was approximated using the average radius (R_i) of the spherical particles composing phase i[76] according to the following equation:

$$\tau_{i,m} = 1 - 1.450(\mu_i - \mu_m)R_i + 1.426[(\mu_i - \mu_m)R_i]^2 \tag{3}$$

This correction is complex to quantify because of the difficulty to estimate R_i. In this work, R_i was estimated with a measurement of the particle size distribution of the CuO and Fe$_2$O$_3$ powders, carried out in a laser diffraction particle size analyzer. The correction was only applied to Fe$_2$O$_3$ because of the high mass absorption coefficient, with R_i = 10 μm.

The overall correction factors used in this work are summarized in Table 3. They lead to an estimation of the x ratio in perfect agreement with the elemental analysis presented in Table 2.
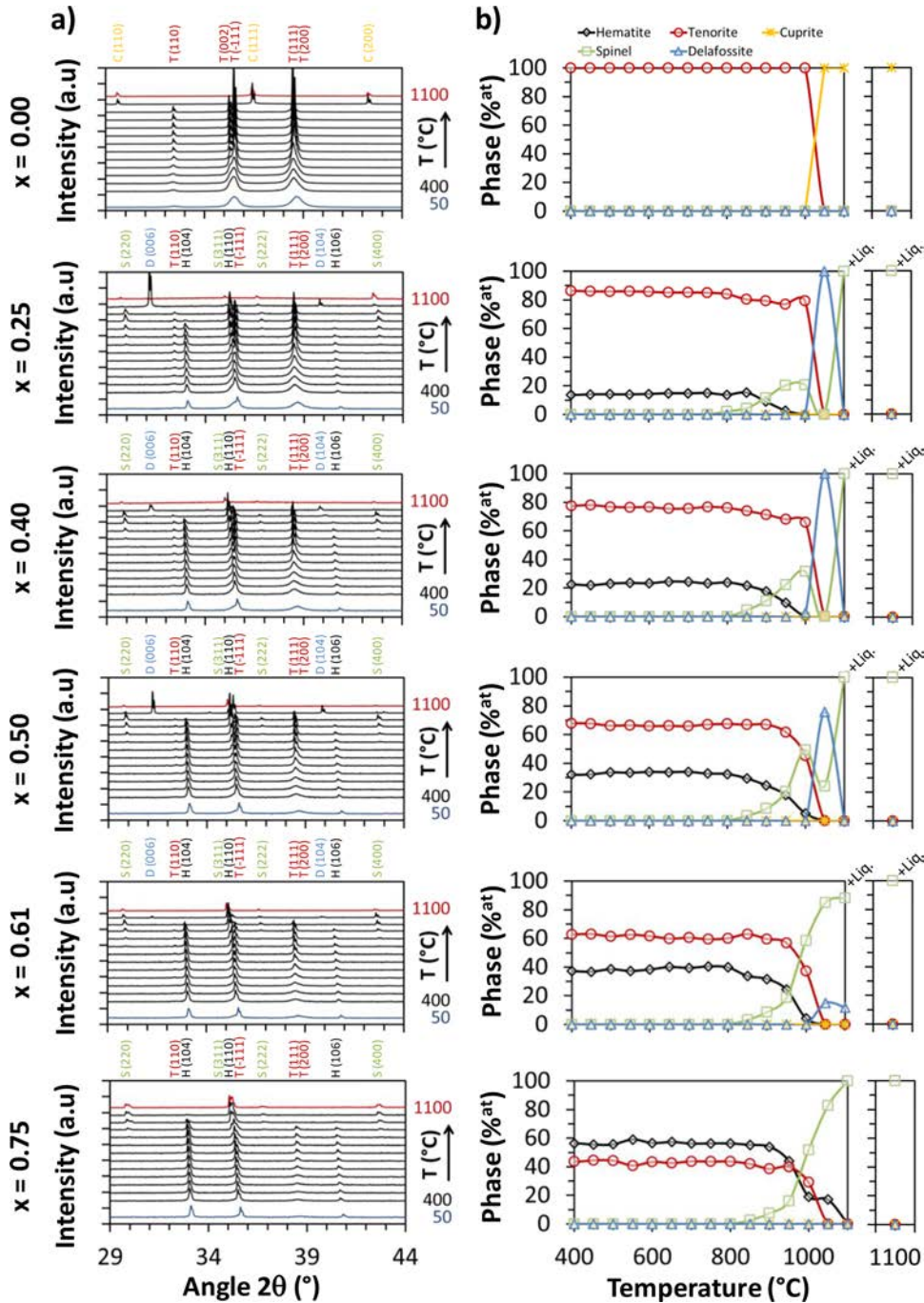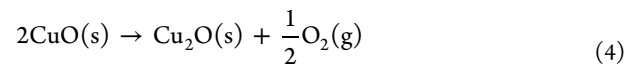
Figure 2. (a) XRD patterns for the samples x = 0.00, 0.25, 0.40, 0.50, 0.61, and 0.75 over the temperature range 50−1100 °C. (b) Corresponding amount of crystalline phases quantified by Rietveld refinement.

3. RESULTS AND DISCUSSION

3.1. Formation Temperature of the Delafossite Phase.
The solid reactions between CuO (tenorite, monoclinic structure, and space group $C2/c$) and α-Fe$_2$O$_3$ (hematite, trigonal structure, and space group $R\bar{3}c$) were evaluated via in situ HT-XRD and Rietveld refinement for all of the samples listed in Table 2. The corresponding HT-XRD patterns are shown in Figure 2a except for x = 1.00 because α-Fe$_2$O$_3$ is stable in the whole range of temperature. The temperature evolution of the amount (in mole percent) of each crystalline phase obtained from Rietveld analysis is plotted in Figure 2b.

For the x = 0.00 sample (pure CuO), a change in the broadening of the tenorite Bragg peaks is visible from 600 °C because of the increase of the particle size (from 45 to >100 nm estimated by Scherrer's law on the one side and laser diffraction particle size analysis on the other side). The complete reduction of tenorite CuO into cuprite Cu$_2$O occurs between 1000 and 1050 °C according to eq 4:

$$2CuO(s) \rightarrow Cu_2O(s) + \frac{1}{2}O_2(g) \tag{4}$$

For all of the samples in the $0.25 \leq x \leq 0.75$ composition range, the single oxide precursors CuO and Fe$_2$O$_3$ are stable up to 800 °C. From 850 to 1000 °C, the precursors react and
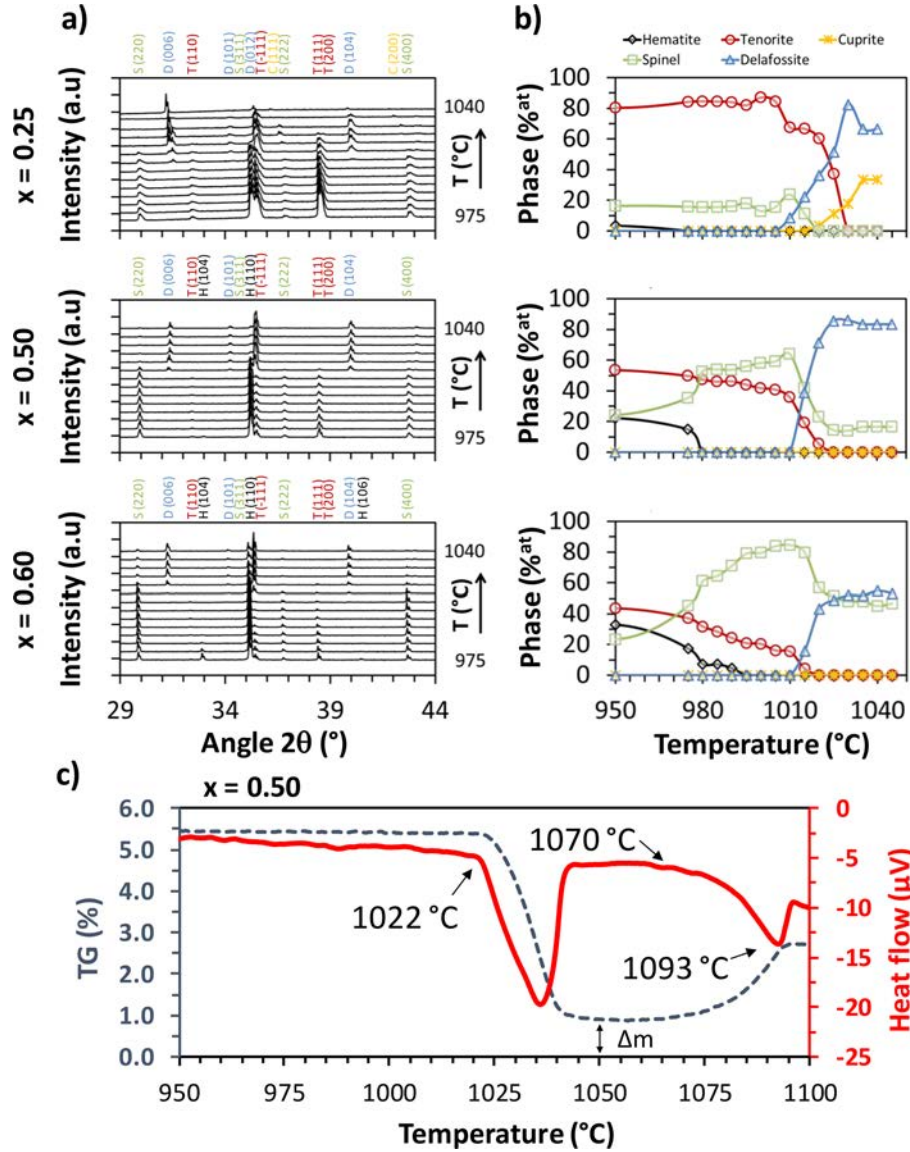
Figure 3. (a) XRD patterns for the samples x = 0.25, 0.50, and 0.60 over the temperature range 975−1045 °C from simple oxides. (b) Corresponding amount of crystalline phases quantified by Rietveld refinement. (c) Mass variation (dotted line) and heat flow (solid line) to pure $CuFeO_2$ in air, over the temperature range 950−1100 °C.

form a spinel phase (green square symbols in Figure 2b), according to eq 5:

$$CuO(s) + Fe_2O_3(s) \rightarrow CuFe_2O_4(s) \tag{5}$$
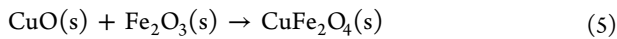
The progressive increase of the amount of the spinel phase from 850 to 1000 °C, which is thermodynamically stable at lower temperature according to the phase diagram (Figure 1), indicates a thermally activated diffusion process. For the samples x = 0.25, 0.40, 0.50, and 0.61, the refined lattice parameter of the spinel phase is constant whatever the Cu content such as, for instance, a = 8.499(2) Å at 950 °C. This corresponds to formation of the stoichiometric $CuFe_2O_4$ cuprospinel phase, in accordance with the phase diagram.

The delafossite phase $CuFeO_2$ forms between 1000 and 1050 °C for $0.25 \leq x \leq 0.61$. The proposed reaction is the concomitant reduction of the Cu^{2+} cations present in the cuprite and spinel phases, according to eq 6. This is confirmed by the significant decrease of the amount of spinel and cuprite

phases at this temperature as observed, for instance, for x = 0.40.

$$CuFe_2O_4(s) + CuO(s) \rightarrow 2CuFeO_2(s) + \frac{1}{2}O_2(g) \tag{6}$$

Because the diffusion process is very active at this temperature, formation of the delafossite phase could also be due to the simultaneous reduction of Cu^{2+} from CuO to Cu_2O (eq 4) and its diffusion within Fe_2O_3 according eq 7.

$$Cu_2O(s) + Fe_2O_3(s) \rightarrow 2CuFeO_2(s) \tag{7}$$
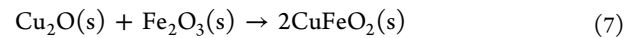
Because no trace of Cu_2O was detected by HT-XRD in the whole series of samples (except for x = 0.00), it can be deduced that the reaction scheme that leads to the formation of delafossite is eqs 5 and 6 rather than eqs 4 and 7.

Finally, at 1100 °C, the delafossite phase fully decomposes. In the samples x = 0.25, 0.40, 0.50, and 0.61, the presence of a liquid phase was observed on top of a spinel phase, as reported in Figure 2b. Even if HT-XRD cannot directly evidence and
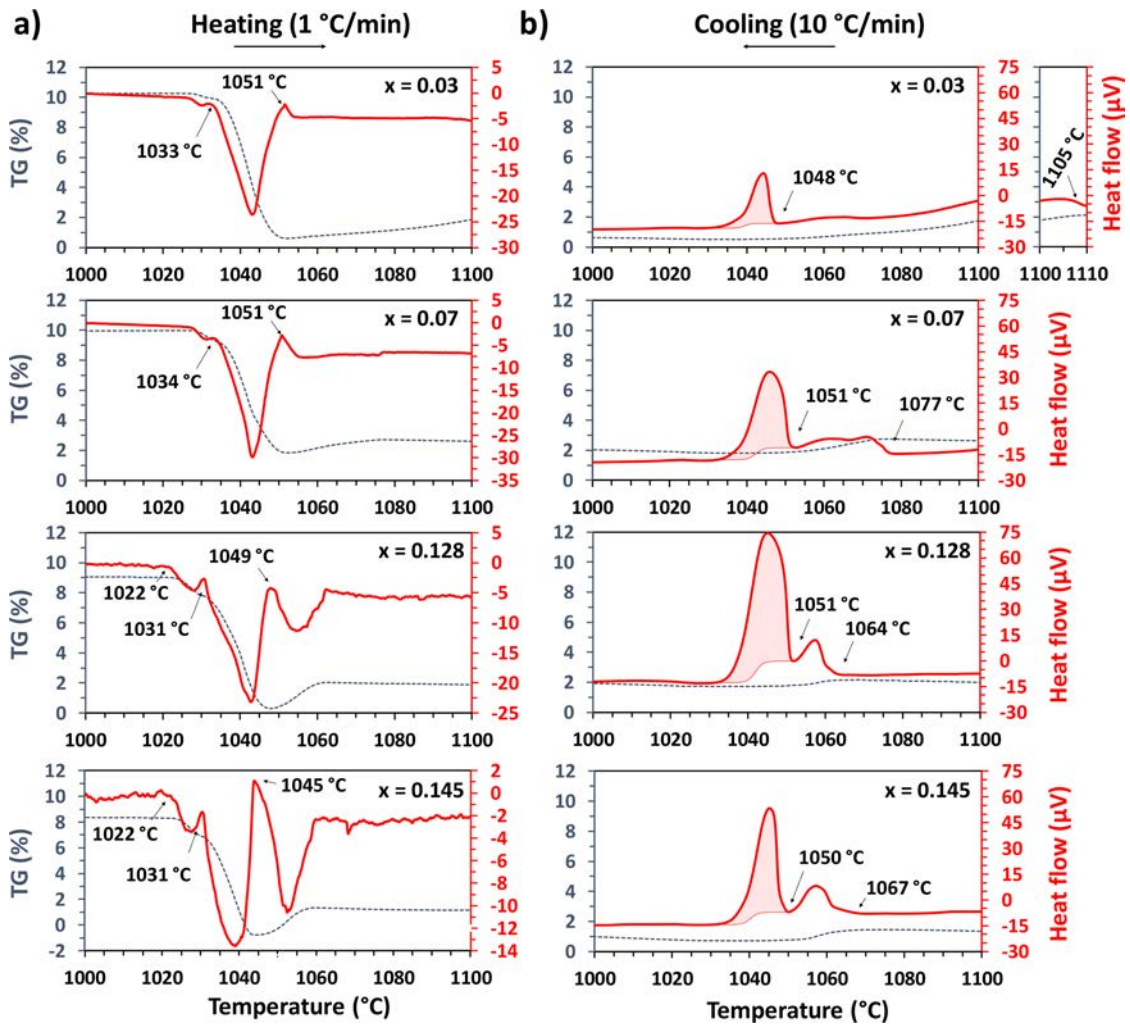
Figure 4. Mass variation (dotted lines) and heat flow (solid lines) over the temperature range 1000−1100 °C: (a) $x = 0.03$, 0.07, 0.128, and 0.145 in air, with a heating rate of 1 °C/min; (b) $x = 0.03$, 0.07, 0.128, and 0.145 in air, with a cooling rate of 10 °C/min. The integral of the peaks associated with eutectic solidification is the red area with a sigmoidal baseline.
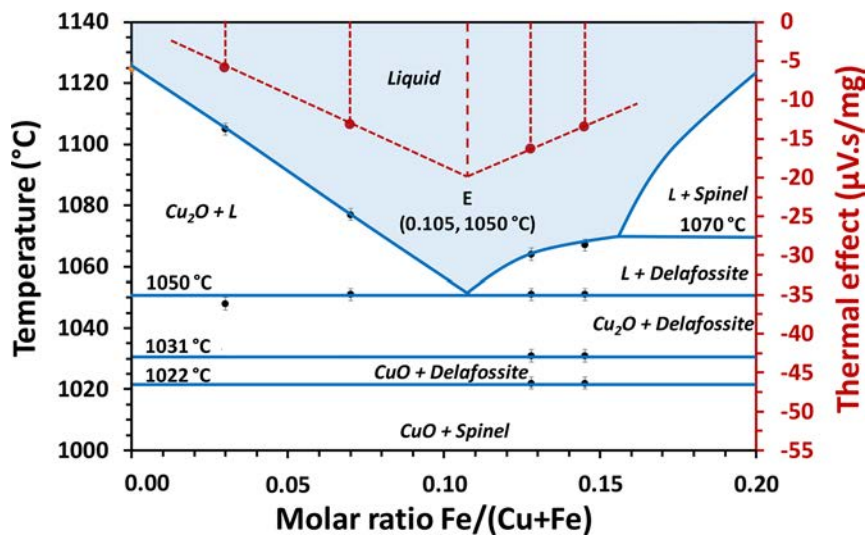

Figure 5. Summary of the experimental information obtained by TGA/DTA: temperature of formation to $CuFeO_2$ at 1022 ± 2 °C; transformation of CuO into Cu_2O at 1031 ± 2 °C; liquidus formation at 1050 ± 2 °C; solidus thermal effect of the eutectic formation during cooling (Tammann's triangle).
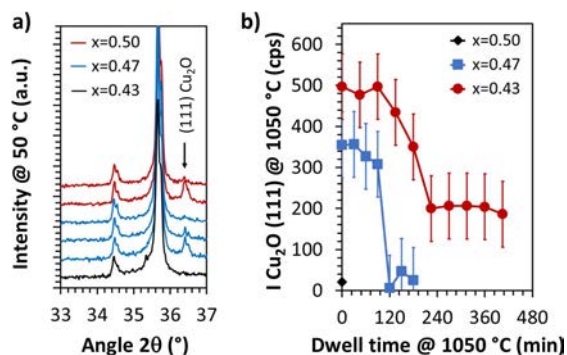
Figure 6. (a) XRD patterns at 50 °C under a nitrogen atmosphere of pure $CuFeO_2$ ($x = 0.50$) and $CuFeO_2$ with spike additions of Cu_2O ($x = 0.47$ and 0.43) after various annealing times at 1050 °C. (b) Intensity of the $Cu_2O(111)$ Bragg peak at 1050 °C versus annealing time.

Table 4. Relationship between the Structural Parameters of Delafossite and Composition

	$CuFeO_2$ ($x = 0.50$)	$CuFe_{0.88}O_2$ ($x = 0.47$)	$D + Cu_2O$ ($x = 0.43$)
	Parameter Cell (Å)		
a	3.0348(5)	3.0349(5)	3.051(5)
c	17.157(3)	17.159(3)	17.161(3)
	Lattice Volume (Å³)		
V	136.85(2)	136.88(2)	136.91(2)
O_2	0.1139(7)	0.1113(5)	0.1112(7)
	Distance (Å)		
Cu−O	1.954(12)	1.910(9)	1.908(12)
Fe−O	1.972(6)	1.993(4)	1.994(6)
	Angle (deg)		
O−Fe−O$_i$	100.6(2)	99.2(2)	99.1(2)
O−Fe−O$_{iv}$	79.4(5)	80.8(4)	80.9(5)
Cu−O−Fe	117.3(4)	118.5(4)	118.5(4)

quantify the presence of a liquid phase, the change of the zero shift and background level of the diffractograms, as well as the visual observation of the crucible after cooling, were considered to be indirect evidence. One can note that when the liquid phase forms, the overall composition of the solid phase is affected. Because this amount was not quantifiable with Rietveld refinement, this was not taken into account but simply notified in Figure 2b.

Because of kinetic limitations in the solid-state reactions such as, for instance, for the spinel phase formation, which only occurs at 800−850 °C for all sample compositions, the amount of each phase evaluated by HT-XRD does not reflect the thermodynamic equilibrium. However, these data are of great support to identify and validate the transition temperatures between phases, especially the appearance (below 1050 °C) and disappearance (above 1050 °C) of the delafossite phase.

In order to determine more accurately the temperature of formation of the delafossite phase, additional HT-XRD measurements were carried out for three mixtures ($x = 0.25$, 0.50, and 0.61) with temperature steps of 5 °C between 975 and 1045 °C. The value of 5 °C corresponds to the minimum applicable temperature step given the accuracy of the temperature probe and thermal regulation in the HT-XRD chamber. The compilation of the resulting phase assemblage is presented in Figure 3, with the HT-XRD patterns in Figure 3a and the temperature evolution of the amount (in mole

percent) of each crystalline phases obtained from Rietveld analysis in Figure 3b.

On the basis of these accurate HT-XRD measurements, the formation temperature of delafossite $CuFeO_2$ can be refined in the temperature range 1010−1015 °C, which is in good agreement with the value of 1015(2) °C[25] published by Yamaguchi. Compared to the first set of experiments (Figure 2), the delafossite formation occurs in a very narrow temperature range (less than 25 °C). This is attributed to the decrease of the overall heating rate from 1.67 °C/min in Figure 2 to 0.0625 °C/min in Figure 3. Another consequence of the decrease of the heating rate is the evidence of Cu_2O formation at around 1030−1040 °C, for the Cu-rich sample $x = 0.25$.

For the sample $x = 0.50$, in the 1020−1045 °C range, the delafossite is not the only phase because around 15 mol % of the spinel phase is present. The origin of this spinel phase may be due to either a slight Fe enrichment on the nominal composition (precisely, $x_{real} = 0.54$) or the presence of an excess of Cu in the delafossite phase ($Cu_{1+y}FeO_2$). These two hypotheses, leading to an excess of Fe in the extra phase, could be at the origin of stabilization of the spinel phase. This also could be due to an equilibrium between $CuFeO_2$ and $CuFe_5O_8$, a spinel phase composed of Cu^+.

The determination of transition temperatures by HT-XRD exhibits a significant uncertainty (± 10 °C) because of the thermal regulation, temperature probes, and kinetics of phase transitions. As a consequence, these experiments were completed by TGA/DTA measurements performed between room temperature and 1100 °C, in air, with a heating rate of 5 °C/min. Pure delafossite $CuFeO_2$ was used to determine its temperature of formation in air. The recorded TGA/DTA signals during heating at above 950 °C are presented in Figure 3c. At low temperature (about 400 °C, not shown here), the initial $CuFeO_2$ powder oxidizes into a stoichiometric spinel and CuO according to eq 8.

$$CuFeO_2(s) + \frac{1}{4}O_2(g) \rightarrow \frac{1}{2}CuFe_2O_4(s) + \frac{1}{2}CuO(s)$$

(8)
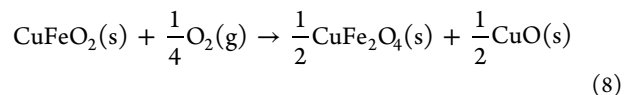
As illustrated in Figure 3c (TGA, blue solid line), the weight gain measured around 1000 °C, related to eq 8, is 5.2%, which corresponds exactly to the theoretical mass gain (5.23%). A first endothermic peak associated with the start of a weight loss is evidenced at 1022 ± 2 °C. This peak is attributed to the delafossite phase formation according to eq 6. However, a residual mass gain of 0.70 wt % can be noted after this reaction. It can be explained by an increase of the O off-stoichiometry $\delta = 0.066$ in $CuFeO_{2+\delta}$ (see a preliminary discussion in section 1.2). This hypothesis is supported by the larger a lattice parameter observed at high temperature ($a = 3.035$ Å at 50 °C and 3.074 Å at 1050 °C), which allows an easier insertion of the O anions into the Cu planes of the structure. A second endothermic peak, attributed to $CuFeO_2$ incongruent melting into spinel and liquid phases, starts at 1070 ± 2 °C and ends at 1093 ± 2 °C. It is associated with a total weight gain of about 1.8% at 1093 °C.

In summary, coupled HT-XRD and TGA/DTA allow one to determine the delafossite formation temperature at 1022 ± 2 °C and its decomposition at 1070 ± 2 °C. These new experimental data strengthen the selection of Shishin et al.[33] for the formation temperature (1019 °C), while we
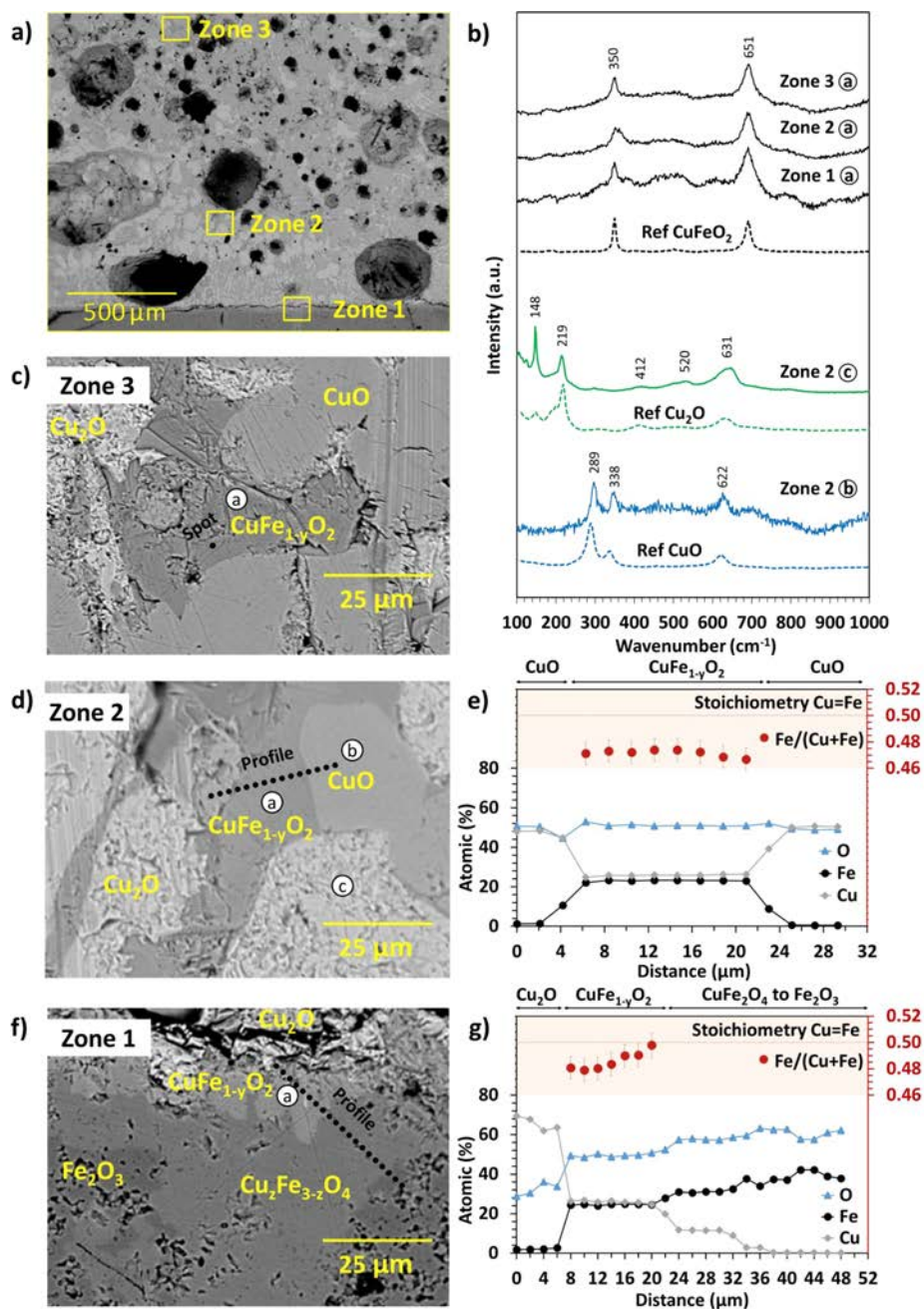
Figure 7. (a) SEM image in the chemical contrast (BSE) mode with three highlighted zones containing the delafossite phase. (b) Micro-Raman spectra of three delafossite zones indicated as in part a, in the BSE images, and of the phases CuO and Cu_2O. (c) BSE image of zone 3. (d) BSE image of zone 2. (e) EPMA profile across the delafossite grain in zone 2. (f) BSE image of zone 1. (g) EPMA profile across Cu_2O, delafossite, and spinel in zone 1.

recommend a slightly lower value than their selected decomposition temperature (1077 °C).

3.2. Eutectic Coordinates. Cu-rich samples (x = 0.00−0.20) were carefully analyzed in order to determine the formation temperature of $CuFeO_2$, Cu_2O, and liquid phases and provide a reliable measurement of the eutectic coordinates. The weight losses and heat flows recorded by TGA/DTA of samples x = 0.03, 0.07, 0.128, and 0.145 in air, with a heating rate of 1 °C/min and a cooling rate of 10 °C/min in Al_2O_3 crucible, are presented in Figure 4. For these measurements, the $CuFeO_2$ and Cu_2O starting materials were used to avoid any kinetic limitation that could lead to a shift of the transition temperatures. Because it is known that the presence of liquid

CuO_x in contact with Al_2O_3 crucibles can form the parent delafossite compound $CuAlO_2$, it is important, in the present study, to ensure that the formation of this phase is limited. Recent works on the formation of $CuAlO_2$ in air[77] and the solubility of Al_2O_3 in CuO_x[78] indicate that $CuAlO_2$ is solid below 1238 °C and that the solubility of Al_2O_3 in CuO_x is limited to 0.11 wt % at 1150 °C. The very limited reactivity between the liquid phase and crucible was confirmed by the complete absence of $CuAlO_2$ in the XRD pattern and subsequent EPMA of the samples.

Parts a and b of Figure 4 show the TGA/DTA signals recorded for Cu-rich samples (x = 0.03, 0.07, 0.128 and 0.145), which contain an increasing amount of $CuFeO_2$ in the starting

powders. Three endothermic peaks are evidenced in all thermograms. The first endothermic peak at around 1022 °C is attributed to the delafossite formation in good agreement with the pure $CuFeO_2$ phase ($x = 0.50$) shown in Figure 3c. This transition temperature is clearly visible on the Fe-rich samples ($x = 0.128$ and 0.145), in contrast to the Cu-rich samples ($x = 0.03$ and 0.07), where the quantity of produced phase is too low to generate an intense signal. The second endothermic peak at $(1031-1034) \pm 2$ is also associated with a weight loss. According to the literature data,[79] it corresponds to the reduction of Cu^{2+} to Cu^+ from CuO to Cu_2O (eq 4). The third endothermic peak is detectable at $(104-10515) \pm 2$ °C, with a slight weight gain. This latter peak is associated with formation of the liquid phase, at a temperature considerably lower than that previously measured (1090 ± 5[25]). The slight weight gain, previously reported by Wolff et al.[77] in a similar system where the liquid contained two oxidation states of Cu (Cu^{2+}/Cu^+), is attributed to the partial oxidation of Cu^+ to Cu^{2+} and the associated O incorporation. The liquid phase was also analyzed during cooling (Figure 4b); values between 1048 and 1051 °C were measured to the exothermic picture of eutectic solidification, in good agreement with the values recorded upon heating. In the case of the eutectic's temperature determination, one value was discarded out of the eight obtained (which corresponds to one measured temperature during heating and one during cooling for each of the four samples). The average of the seven selected measurements led to $T = 1050.1$ °C with an uncertainty of 1.7 °C. Our recommended value is $T_{eutectic} = 1050 \pm 2$ °C because it is in the reliability range of expanded uncertainty, using a coverage factor of 2.45 with a level of confidence of 95%.

The other information extracted from the cooling curves is the solidus temperature measured at 1105, 1077, 1064, and 1067 ± 2 °C for samples $x = 0.03$, 0.07, 0.128, and 0.145, respectively. Tammann's triangle method, which is based on analysis of the thermic effect of the eutectic formation, was used to determine the eutectic composition. The integrated surfaces of the DTA peaks represented as the red area in Figure 4b were plotted versus composition for the samples $x = 0.03$, 0.07, 0.128, and 0.145. The experimental information is summarized in Figure 5 with extrapolation of the thermic effect of eutectic formation in cooling. The intersection of both sides of the triangle at $x = 0.105$ mol % represents our best estimation of the eutectic composition.

3.3. Cationic Nonstoichiometry in Delafossite. *HT-XRD Characterization of Stoichiometric $CuFeO_2$ + Minor Additions of CuO.* Compositions close to the delafossite phase, i.e., with $x \approx 0.50$, were also analyzed by HT-XRD with steps of 5 °C between 975° and 1045 °C in order to study the possible cationic nonstoichiometry range $Cu_{1\pm y}Fe_{1\pm y}O_2$. Starting from the CuO and Fe_2O_3 precursors, a spinel phase is systematically formed together with the delafossite phase when the initial stoichiometry contains an excess of Fe, i.e., when $x > 0.50$, such as, for instance, for $x = 0.60$ (Figure 2) or $x = 0.52$ (not shown here). In contrast, for $x < 0.50$, the delafossite phase is the only phase detected by XRD, such as, for instance, with the sample $x = 0.40$ at 1050 °C (Figure 2). However, as previously mentioned, in this part of the diagram, the phase assemblage can not be precisely quantified by Rietveld analysis because of the formation of a Cu-rich liquid phase ($x \approx 0.105$). Because quantification of the amount of liquid phase is not possible, the amount and composition of delafossite cannot be determined either.

To overcome this difficulty, we carried out three successive HT-XRD analyses on (1) a stoichiometric delafossite $CuFeO_2$ ($x = 0.50$) sample, (2) the same sample with the addition of Cu_2O, leading to the composition $x = 0.47$, and (3) the same sample once again enriched in Cu_2O, leading to the composition $x = 0.43$. Furthermore, during the HT-XRD recordings, a nitrogen atmosphere was continuously maintained in the chamber in order to stabilize the Cu^+ valence and to avoid any decomposition of the delafossite phase at 1050 °C.

Figure 6a shows the XRD patterns at 50 °C of various compositions after thermal cycles at a maximal temperature of 1050 °C: the pristine stoichiometric $x = 0.50$ $CuFeO_2$ material after 1 cycle, the mixture $x = 0.47$ (i.e., $CuFeO_2$ + 6 mol % Cu_2O) before and after 2 cycles, and the mixture $x = 0.43$ [i.e., $CuFeO_2$ + (6 + 7) mol % Cu_2O] before and after 1 cycle. Figure 6b shows the evolution of the intensity of the $Cu_2O(111)$ characteristic Bragg peak at 1050 °C during the dwells. The error bars correspond to the accuracy of the intensity measurement in the HT-XRD setup for scans of 30 and 45 min. This (111) peak appears at around 36.5° in 2θ at room temperature, as shown in Figure 6a.

The pure delafossite was first submitted to a thermal cycle up to 1050 °C. It confirms its stability under a nitrogen atmosphere, over the temperature range 50−1050 °C. Furthermore, the delafossite phase is pure, without any trace of Cu_2O or any other phase (black pattern in Figure 6a). The resulting Cu_2O intensity (20 cps) measured at 1050 °C and reported with a black diamond in Figure 6b is not significant and is attributed to statistical accumulation. The addition of 6 mol % Cu_2O is detected on the XRD pattern at 50 °C (the first blue pattern in Figure 6a) and confirmed by a measurable intensity at 1050 °C (blue squares in Figure 6b). After two temperature cycles and 180 min of cumulative dwell time at 1050 °C, the peak disappears, indicating that Cu_2O diffused in the delafossite phase.

A second addition of 7 mol % Cu_2O was then realized. The characteristic $Cu_2O(111)$ peak is again clearly identifiable (the first red pattern in Figure 6a). A dwell of 240 min at 1050 °C leads to a partial extinction of the signal (red circles in Figure 6b). However, even after a total dwell time of 400 min, the peak intensity remains constant, indicating the presence of Cu_2O as a stable phase in the system. Back to 50 °C, the $Cu_2O(111)$ peak is still visible (the second red pattern in Figure 6a).

This set of experiments proves that the delafossite can accept an excess of Cu in a range of compositions between $x = 0.47$ and 0.43.

Rietveld analysis carried out on the samples $x = 0.50$, 0.47, and 0.43 after their respective annealing at 1050 °C led to the structural parameters listed in Table 4. These data are fully consistent with the literature data reported in Table 1, and no clear change in the lattice constant can be associated with the Cu enrichment of the system. One can only notice some slight changes in the Cu−O and Fe−O distances (decrease of the Cu−O bond length from 1.95 to 1.91 Å and concomitant increase of the Fe−O length from 1.97 to 1.99 Å) in the delafossite structure from $x = 0.50$ to 0.47. No changes are evident from $x = 0.47$ to 0.43. This confirms the hypothesis of Cu enrichment into the delafossite phase up to $x = 0.47$.

EPMA on the Diffusion Couple. EPMA was carried out in order to improve quantification of the nonstoichiometry range of the delafossite phase, thanks to a specific diffusion couple between CuO and Fe_2O_3 oxides.

The diffusion couple (see section 2.1 for the preparation protocol) allows one to obtain a material containing different zones, whereas the composition varies from the initial pure CuO and Fe_2O_3 to various mixtures of both oxides. Figure 7a shows the SEM image of the diffusion couple in a chemical contrast (backscattered electron, BSE) mode with the initial CuO/Fe_2O_3 interface in the lower part. Because of the elaboration conditions close to the melting temperature of the Cu compounds, the specimen exhibits large porosities in the Cu-rich region, which appears as big dark areas. Three representative zones containing the delafossite phase are also presented, which are all located in the Cu-rich region. The first region (zone 1) is located at the initial CuO/Fe_2O_3 interface, the second one (zone 2) is located at around 400 μm from the interface, and the last one (zone 3) is located at more than 1300 μm from the interface. The overall Cu (Fe) content is increasing (decreasing) from zone 1 to zone 3.

The BSE image of the Cu-richest zone (zone 3) is shown in Figure 7c. It exhibits three different chemical contrasts, i.e., three different phases (delafossite, cuprite, and tenorite) because of variation of their average atomic numbers. A 0D-point EPMA measurement of the dark-gray area leads to 26.3(6) mol % Cu, 23.2(6) mol % Fe, and 50.5(6) mol % O. It corresponds to the formula $CuFe_{0.88}O_{1.92}$. EPMA indicates that the light-gray and white areas correspond to pure CuO and Cu_2O, respectively, in good agreement with the electronic density. The BSE image of zone 2 (Figure 7d) shows similar areas, i.e., a homogeneous grain of the delafossite phase surrounded by the Cu_2O and CuO phases. The average composition of delafossite (Figure 7e) determined by 1D-line analysis in EPMA is 25.9(4) mol % Cu, 23.2(4) mol % Fe, and 50.9(13) mol % O. The normalized formula for delafossite in this region is $CuFe_{0.89}O_{1.96}$. This composition is homogeneous from side to side on the grain. The interface zone (zone 1) presents a Cu_2O grain (white area) with around 1.9% Fe solubilized (analysis from 0 to 6 μm; see Figure 7f). At 8 μm from the starting point, a delafossite grain is analyzed. In this grain, a clear evolution of the x ratio is observed from $x = 0.48$ on the Cu-rich side (distance = 8 μm) to $x = 0.50$ on the Fe-rich side (distance = 20 μm). The latter reaches the stoichiometric composition $x = 0.50$ at the interface with a grain composed of a spinel solid solution $Cu_zFe_{3-z}O_4$. The maximal off-stoichiometry detected in the sample was in zone 3. For this composition, the Fe/(Cu + Fe) molar ratio is $x = 0.47$. This minimal Fe content is in accordance with HT-XRD experiments.

In order to determine if the area in which the chemical analysis shows a deficient Cu content corresponds to a pure nonstoichiometric delafossite or a mixture of stoichiometric delafossite ($CuFeO_2$) and copper oxide phase (CuO or Cu_2O), micro-Raman characterizations have been carried out in the same area. Beforehand, various reference spectra have been acquired on pure CuO, Cu_2O, and $CuFe_2O_4$ powders (Figure 7b). In parts c, d, and f of Figure 7 respectively related to zones 3, 2, and 1, the label "a" indicates the areas identified as the delafossite phase in which the Raman measurements were made. Raman spectra have been acquired very closed to the area where the chemical analysis has been carried out. The resulting spectra are shown in Figure 7b and compared to that

obtained on the pure $CuFeO_2$ powder. This analysis confirms the presence of pure delafossite in the three zones, with no presence of copper oxides (CuO or Cu_2O). In zone 2, two other Raman measurements have been made in the areas b and c, which confirms that the CuO and Cu_2O phases are clearly identified and fit well with the chemical analysis.

These coupled EPMA/SEM/Raman analyses prove that the delafossite structure could accommodate some Cu excess up to $x = 0.47$, i.e., with a $CuFe_{0.88}O_{2-\delta}$ formula.

4. CONCLUSION

In this work, we reinvestigated the Cu−Fe−O system in air with a special focus on the delafossite phase. The starting point
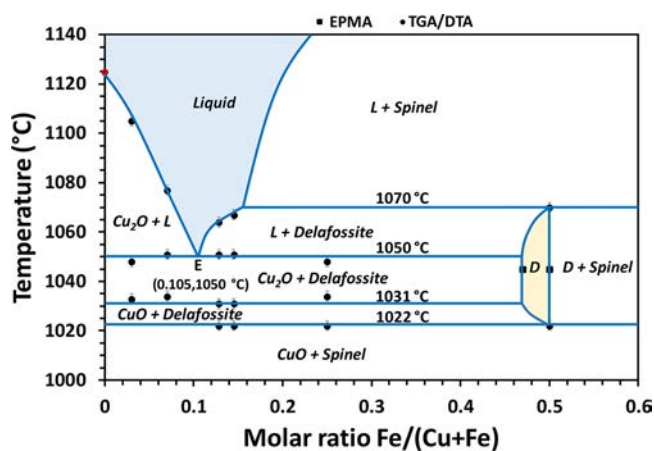
Figure 8. Experimental phase diagram of the Cu−Fe−O system in air obtained in this work, with experimental points with an accuracy of ±2 °C for the transition temperatures.

of this study was the phase diagrams available in the literature (Perrot et al.,[31] Khvan et al.,[32] and Shishin et al.[33]). Some inconsistencies were highlighted, especially regarding the delafossite stability range and the eutectic point coordinates. Besides, considering the composition of $CuFeO_2$, no work had so far provided real evidence about the existence of a cationic off-stoichiometry in this compound.

We performed a systematic experimental study of the full system under air between 50 and 1100 °C by in situ HT-XRD and TGA/DTA, and EMPA was performed to investigate the delafossite composition stability range in the copper−iron mixed oxide regions.

The stability region of delafossite was successfully determined in air, with a formation temperature at 1022 ± 2 °C and an incongruent decomposition at 1070 ± 2 °C. DTA curves were used to measure the liquidus temperature at 1050 ± 2 °C with a eutectic composition at $x = 0.105$ obtained by Tammann's triangle method.

For the first time, a cationic off-stoichiometry of cuprous ferrite $CuFe_{1-y}O_{2-\delta}$ was evidenced, with a maximum value of $y = 0.12$ measured by EPMA, this value being supported by HT-XRD analysis. No evidence of an Fe-rich delafossite was found, and complementary analysis under a controlled atmosphere shows narrow lattice variation with an increase of Cu in the delafossite structure. The updated experimental phase diagram obtained as a result of this work is presented in Figure 8 with experimental points.

■ AUTHOR INFORMATION

Corresponding Author
*E-mail: barnabe@chimie.ups-tlse.fr.

ORCID ⓘ
Laurent Cassayre: 0000-0001-6876-6086
Antoine Barnabé: 0000-0001-8570-3570

Notes
The authors declare no competing financial interest.

■ REFERENCES

(1) Kulkarni, A. D. The Thermodynamic Studies of Liquid Copper Alloys by Electromotive Force Method: Part I. The Cu-O, Cu-Fe-O, and Cu-Fe Systems. *Metall. Trans. A* **1973**, *4* (7), 1713−1721.

(2) Sahu, S. K.; Navrotsky, A. Thermodynamics of Copper-Manganese and Copper-Iron Spinel Solid Solutions. *J. Am. Ceram. Soc.* **2017**, *100* (8), 3684−3692.

(3) Kameoka, S.; Tanabe, T.; Tsai, A. P. Spinel $CuFe_2O_4$: A Precursor for Copper Catalyst with High Thermal Stability and Activity. *Catal. Lett.* **2005**, *100* (1−2), 89−93.

(4) Du, X.; Wang, C.; Chen, M.; Jiao, Y.; Wang, J. Electrochemical Performances of Nanoparticle Fe_3O_4/Activated Carbon Super-capacitor Using KOH Electrolyte Solution. *J. Phys. Chem. C* **2009**, *113* (6), 2643−2646.

(5) Estrella, M.; Barrio, L.; Zhou, G.; Wang, X.; Wang, Q.; Wen, W.; Hanson, J. C.; Frenkel, A. I.; Rodriguez, J. A. In Situ Characterization of $CuFe_2O_4$ and Cu/Fe_3O Water−Gas Shift Catalysts. *J. Phys. Chem. C* **2009**, *113* (32), 14411−14417.

(6) Yeste, M. P.; Vidal, H.; García-Cabeza, A. L.; Hernández-Garrido, J. C.; Guerra, F. M.; Cifredo, G. A.; González-Leal, J. M.; Gatica, J. M. Low Temperature Prepared Copper-Iron Mixed Oxides for the Selective CO Oxidation in the Presence of Hydrogen. *Appl. Catal., A* **2018**, *552*, 58.

(7) Zhou, G.; Wang, D.-W.; Li, F.; Zhang, L.; Li, N.; Wu, Z.-S.; Wen, L.; Lu, G. Q.; Cheng, H.-M. Graphene-Wrapped Fe_3O_4 Anode Material with Improved Reversible Capacity and Cyclic Stability for Lithium Ion Batteries. *Chem. Mater.* **2010**, *22* (18), 5306−5313.

(8) Cama, C. A.; Pelliccione, C. J.; Brady, A. B.; Li, J.; Stach, E. A.; Wang, J.; Wang, J.; Takeuchi, E. S.; Takeuchi, K. J.; Marschilok, A. C. Redox Chemistry of a Binary Transition Metal Oxide (AB_2O_4): A Study of the Cu^{2+}/Cu^0 and Fe^{3+}/Fe^0 Interconversions Observed upon Lithiation in a $CuFe_2O_4$ Battery Using X-Ray Absorption Spectros-copy. *Phys. Chem. Chem. Phys.* **2016**, *18* (25), 16930−16940.

(9) Tao, S.; Gao, F.; Liu, X.; Toft Sørensen, O. Preparation and Gas-Sensing Properties of $CuFe_2O_4$ at Reduced Temperature. *Mater. Sci. Eng., B* **2000**, *77* (2), 172−176.

(10) Figuerola, A.; Di Corato, R.; Manna, L.; Pellegrino, T. From Iron Oxide Nanoparticles towards Advanced Iron-Based Inorganic Materials Designed for Biomedical Applications. *Pharmacol. Res.* **2010**, *62* (2), 126−143.

(11) Costa, A. F.; Pimentel, P. M.; Aquino, F. M.; Melo, D. M. A.; Melo, M. A. F.; Santos, I. M. Gelatin Synthesis of $CuFe_2O_4$ and $CuFeCrO_4$ Ceramic Pigments. *Mater. Lett.* **2013**, *112*, 58−61.

(12) Friedel, C. Sur Une Combinaison Naturelle Des Oxydes de Fer et de Cuivre et Sur La Reproduction de l'atacamite. *C. R. Hebd. Seances Acad. Sci.* **1873**, *1*, 211−214.

(13) Kawazoe, H.; Yasukawa, M.; Hyodo, H.; Kurita, M.; Yanagi, H.; Hosono, H. P-Type Electrical Conduction in Transparent Thin Films of $CuAlO_2$. *Nature* **1997**, *389* (6654), 939−942.

(14) Wuttig, A.; Krizan, J. W.; Gu, J.; Frick, J. J.; Cava, R. J.; Bocarsly, A. B. The Effect of Mg-Doping and Cu Nonstoichiometry on the Photoelectrochemical Response of $CuFeO_2$. *J. Mater. Chem. A* **2017**, *5* (1), 165−171.

(15) Prévot, M. S.; Guijarro, N.; Sivula, K. Enhancing the Performance of a Robust Sol-Gel-Processed p-Type Delafossite $CuFeO_2$ Photocathode for Solar Water Reduction. *ChemSusChem* **2015**, *8* (8), 1359−1367.

(16) Prévot, M. S.; Jeanbourquin, X. A.; Bourée, W. S.; Abdi, F.; Friedrich, D.; van de Krol, R.; Guijarro, N.; Le Formal, F.; Sivula, K. Evaluating Charge Carrier Transport and Surface States in $CuFeO_2$ Photocathodes. *Chem. Mater.* **2017**, *29* (11), 4952−4962.

(17) Oh, Y.; Yang, W.; Kim, J.; Jeong, S.; Moon, J. Enhanced Photocurrent of Transparent $CuFeO_2$ Photocathodes by Self-Light-Harvesting Architecture. *ACS Appl. Mater. Interfaces* **2017**, *9* (16), 14078−14087.

(18) Oh, Y.; Yang, W.; Tan, J.; Lee, H.; Park, J.; Moon, J. Photoelectrodes Based on 2D Opals Assembled from Cu-Delafossite Double-Shelled Microspheres for an Enhanced Photoelectrochemical Response. *Nanoscale* **2018**, *10* (8), 3720−3729.

(19) Jang, Y. J.; Park, Y. B.; Kim, H. E.; Choi, Y. H.; Choi, S. H.; Lee, J. S. Oxygen-Intercalated $CuFeO_2$ Photocathode Fabricated by Hybrid Microwave Annealing for Efficient Solar Hydrogen Production. *Chem. Mater.* **2016**, *28* (17), 6054−6061.

(20) Tablero Crespo, C. Potentiality of $CuFeO_2$-Delafossite as a Solar Energy Converter. *Sol. Energy* **2018**, *163*, 162−166.

(21) Ruttanapun, C.; Prachamon, W.; Wichainchai, A. Optoelec-tronic Properties of $Cu_{1−x}Pt_xFeO_2$ ($0 \leq x \leq 0.05$) Delafossite for p-Type Transparent Conducting Oxide. *Curr. Appl. Phys.* **2012**, *12* (1), 166−170.

(22) Ruttanapun, C.; Jindajitawat, P.; Buranasiri, P.; Naenkieng, D.; Boonyopakorn, N.; Harnwunggmoung, A.; Thowladda, W.; Neeyakorn, W.; Thanachayanont, C.; Charoenphakdee, A. Prepara-tion, Characterization and Finite Element Computation of Cu-$(Al_{1/2}Fe_{1/2})O_2$ Delafossite-Oxide Thermoelectric Generator Module. *Integr. Ferroelectr.* **2014**, *156* (1), 102−114.

(23) Rudradawong, C.; Ruttanapun, C. Effect of Excess Oxygen for $CuFeO_{2.06}$ Delafossite on Thermoelectric and Optical Properties. *Phys. B* **2017**, *526* (July), 21−27.

(24) Buist, D. S.; Gadalla, A. M. M.; White, J. Delafossite and the System Cu-Fe-O. *Mineral. Mag. J. Mineral. Soc.* **1966**, *35* (273), 731−741.

(25) Yamaguchi, T. Phase Relations in the Ferrite Region of the System Cu-Fe-O in Air. *Proc. Fujihara Meml. Fac. Eng. Keio Univ.* **1966**, *19* (75), 192−198.

(26) Schaefer, S. C.; Hundley, G. L.; Block, F. E.; McCune, R. A.; Mrazek, R. V. Phase Equilibria and X-Ray Diffraction Investigation of the System Cu-Fe-O. *Metall. Trans.* **1970**, *1*, 2557−2563.

(27) Jacob, K. T.; Fitzner, K.; Alcock, C. B. Activities in the Spinel Solid Solution, Phase Equilibria and Thermodynamic Properties of Ternary Phases in the System Cu-Fe-O. *Metall. Trans. B* **1977**, *8* (2), 451−460.

(28) Zinovik, M. A. The Phase Equilibrium Diagram of the CuO-Cu_2O-Fe_2O_3-Fe_3O_4 System. *Russ. J. Inorg. Chem.* **1988**, *33* (10), 1543−1545.

(29) Oishi, T.; Nakagawa, K.; Ono, K. Phase Diagram and Thermodynamics of the Molten Cu-Fe-O System at 1773 K. *Nippon Kinzoku Gakkaishi* **1989**, *53* (7), 692.

(30) Ristić, M.; Hannoyer, B.; Popović, S.; Musić, S.; Bajraktaraj, N. Ferritization of Copper Ions in the Cu-Fe-O System. *Mater. Sci. Eng., B* **2000**, *77* (1), 73−82.

(31) Perrot, P.; Arnout, S.; Vrestal, J. Copper−Iron−Oxygen. In *Landolt−Börnstein—Group IV Physical Chemistry*; Effenberg, G., Ilyenko, S., Eds.; Springer: Berlin, 2008; Vol. *11D4*.

(32) Khvan, A. V.; Fabrichnaya, O. B.; Savinykh, G.; Adam, R.; Seifert, H. J. Thermodynamic Assessment of the Cu-Fe-O System. *J. Phase Equilib. Diffus.* 2011, 32 (6), 498−511.

(33) Shishin, D.; Hidayat, T.; Jak, E.; Decterov, S. A. Critical Assessment and Thermodynamic Modeling of the Cu-Fe-O System. *CALPHAD: Comput. Coupling Phase Diagrams Thermochem.* 2013, 41, 160−179.

(34) Mexmain, J. Contribution à l'étude Du Ferrite Cuivreux et de Ses Solutions Solide Avec Le Ferrite Cuivrique. *J. Ann. Chim. Vol.* 1971, 6, 297−308.

(35) Kenfack, F.; Langbein, H. Influence of the Temperature and the Oxygen Partial Pressure on the Phase Formation in the System Cu-Fe-O. *Cryst. Res. Technol.* 2004, 39 (12), 1070−1079.

(36) Rogers, A. F. Delafossite, a Cuprous Metaferrite from Bisbee, Arizona. *Am. J. Sci.* 1913, s4−35 (207), 290−294.

(37) Wiedersich, H.; Savage, J. W.; Muir, A. H.; Swarthout, D. G. On Composition of Delafossite. *Mineral. Mag. J. Mineral. Soc.* 1968, 36 (281), 643−650.

(38) Hey, M. H. On Composition of Natural Delafossite. *Mineral. Mag. J. Mineral. Soc.* 1968, 36 (281), 651−653.

(39) Ashmore, N. A.; Cann, D. P. Electrical and Structural Characteristics of Non-Stoichiometric Cu-Based Delafossites. *J. Mater. Sci.* 2005, 40 (15), 3891−3896.

(40) Trari, M.; Töpfer, J.; Dordor, P.; Grenier, J. C.; Pouchard, M.; Doumerc, J. P. Preparation and Physical Properties of the Solid Solutions $Cu_{1+x}Mn_{1-x}O_2$ ($0 \leq x \leq 0.2$). *J. Solid State Chem.* 2005, 178 (9), 2751−2758.

(41) Ling, D. C.; Chiang, C. W.; Wang, Y. F.; Lee, Y. J.; Yeh, P. H. Effect of Cr Deficiency on Physical Properties of Triangular-Lattice Antiferromagnets $CuCr_{1-x}O_2$ ($0 \leq x \leq 0.10$). *J. Appl. Phys.* 2011, 109 (7), 07D908.

(42) Lunca Popa, P.; Crêpellière, J.; Nukala, P.; Leturcq, R.; Lenoble, D. Invisible electronics: Metastable Cu-vacancies chain defects for highly conductive p-type transparent oxide. *Appl. Mater. Today* 2017, 9, 184−191.

(43) Elazhari, M.; Ammar, A.; Elaatmani, M.; Trari, M.; Doumerc, J. P. Oxidation at Low Temperature of Some Delafossite-Type Oxides $CuMO_2$ (M = Sc, Ga, Y, La, Nd, $La_{0.5}Y_{0.5}$). *Eur. J. Solid State Inorg. Chem.* 1997, 34 (5), 503−509.

(44) Garlea, O.; Darie, C.; Bougerol, C.; Isnard, O.; Bordet, P. Structure of $LaCuO_{2.66}$: An Oxidized Delafossite Compound Containing Hole-Doped Kagome Planes of Cu^{2+} Cations. *Solid State Sci.* 2003, 5 (8), 1095−1104.

(45) Mugnier, E.; Barnabé, A.; Tailhades, P. Synthesis and Characterization of $CuFeO_{2+\delta}$ Delafossite Powders. *Solid State Ionics* 2006, 177 (5−6), 607−612.

(46) Zhao, T.-R.; Hasegawa, M.; Takei, H. Oxygen Non-stoichiometry in Copper Iron Oxide $[CuFeO_{2+\delta}]$ Single Crystals. *J. Cryst. Growth* 1997, 181 (1−2), 55−60.

(47) Hasegawa, M.; Batrashevich, M. I.; Zhao, T. R.; Takei, H.; Goto, T. Effects of Oxygen Nonstoichiometry on the Stability of Antiferromagnetic Phases of $CuFeO_{2+x}$ Single Crystals. *Phys. Rev. B: Condens. Matter Mater. Phys.* 2001, 63 (18), 184437.

(48) Trofimov, E. A. Thermodynamic Analysis of Phase Equilibrium in Multicomponent Systems Including Metallic Melts. Doctoral Dissertation, South Ural State University, Chelyabinsk, Russia, 2014.

(49) Shannon, R. D.; Rogers, D. B.; Prewitt, C. T. Chemistry of Noble Metal Oxides. I. Syntheses and Properties of ABO_2 Delafossite Compounds. *Inorg. Chem.* 1971, 10 (4), 713−718.

(50) Shannon, R. D.; Prewitt, C. T.; Rogers, D. B. Chemistry of Noble Metal Oxides. II. Crystal Structures of Platinum Cobalt Dioxide, Palladium Cobalt Dioxide, Coppper Iron Dioxide, and Silver Iron Dioxide. *Inorg. Chem.* 1971, 10 (4), 719−723.

(51) Dordor, P.; Chaminade, J. P.; Wichainchai, A.; Marquestaut, E.; Doumerc, J. P.; Pouchard, M.; Hagenmuller, P.; Ammar, A. Crystal

(52) Mekata, M.; Yaguchi, N.; Takagi, T.; Sugino, T.; Mitsuda, S.; Yoshizawa, H.; Hosoito, N.; Shinjo, T. Successive Magnetic Ordering in $CuFeO_2$ - A New Type of Partially Disordered Phase in a Triangular Lattice Antiferromagnet. *J. Phys. Soc. Jpn.* 1993, 62 (12), 4474−4487.

(53) Zhao, T.; Hasegawa, M.; Takei, H. Crystal Growth and Characterization of Cuprous Ferrite ($CuFeO_2$). *J. Cryst. Growth* 1996, 166 (1−4), 408−413.

(54) Omeiri, S.; Bellal, B.; Bouguelia, A.; Bessekhouad, Y.; Trari, M. Electrochemical and Photoelectrochemical Characterization of $CuFeO_2$ Single Crystal. *J. Solid State Electrochem.* 2009, 13 (9), 1395−1401.

(55) Muir, A. H.; Wiedersich, H. An Investigation of $CuFeO_2$ by the Mössbauer Effect. *J. Phys. Chem. Solids* 1967, 28 (1), 65−71.

(56) Doumerc, J. P.; Ammar, A.; Wichainchai, A.; Pouchard, M.; Hagenmuller, P. Sur Quelques Nouveaux Composes de Structure de Type Delafossite. *J. Phys. Chem. Solids* 1987, 48 (1), 37−43.

(57) Zhao, T. R.; Hasegawa, M.; Kondo, T.; Yagi, T.; Takei, H. X-Ray Diffraction Study of Copper Iron Oxide $[CuFeO_2]$ under Pressures up to 10 GPa. *Mater. Res. Bull.* 1997, 32 (2), 151−157.

(58) Sukeshini, A. M.; Kobayashi, H.; Tabuchi, M.; Kageyama, H. Physicochemical Characterization of $CuFeO_2$ and Lithium Inter-calation. *Solid State Ionics* 2000, 128 (1−4), 33−41.

(59) El Ataoui, K.; Doumerc, J. P.; Ammar, A.; Gravereau, P.; Fournès, L.; Wattiaux, A.; Pouchard, M. Preparation, Structural Characterization and Mössbauer Study of the $CuFe_{1-x}V_xO_2$ ($0 \leq x \leq 0.67$) Delafossite-Type Solid Solution. *Solid State Sci.* 2003, 5 (9), 1239−1245.

(60) Sheets, W. C.; Mugnier, E.; Barnabé, A.; Marks, T. J.; Poeppelmeier, K. R. Hydrothermal Synthesis of Delafossite-Type Oxides. *Chem. Mater.* 2006, 18 (1), 7−20.

(61) Lalanne, M.; Barnabe, A.; Mathieu, F.; Tailhades, P. Synthesis and Thermostructural Studies of a $CuFe_{1-x}Cr_xO_2$ Delafossite Solid Solution with $0 \leq x \leq 1$. *Inorg. Chem.* 2009, 48 (13), 6065−6071.

(62) Pavunny, S. P.; Kumar, A.; Katiyar, R. S. Raman Spectroscopy and Field Emission Characterization of Delafossite $CuFeO_2$. *J. Appl. Phys.* 2010, 107 (1), 013522.

(63) Ruttanapun, C.; Wichainchai, A.; Prachamon, W.; Yangthaisong, A.; Charoenphakdee, A.; Seetawan, T. Thermoelectric Properties of $Cu_{1-x}Pt_xFeO_2$ ($0.00 \leq x \leq 0.05$) Delafossite-Type Transition Oxide. *J. Alloys Compd.* 2011, 509 (13), 4588−4594.

(64) Amrute, A. P.; Łodziana, Z.; Mondelli, C.; Krumeich, F.; Pérez-Ramírez, J. Solid-State Chemistry of Cuprous Delafossites: Synthesis and Stability Aspects. *Chem. Mater.* 2013, 25 (21), 4423−4435.

(65) Kucerova, G.; Ozdín, D. Primary Low-Temperature Delafossite ($CuFeO_2$) from Mine Tailing Slovinky (Slovakia). *Bull. Mineral. Oddel. Nar. Muz. v Praze* 2013, 21 (1), 78−83.

(66) Sarabia, M. A.; Rojas, S. D.; López-Cabaña, Z.; Villalba, R.; González, G.; Cabrera, A. L. Carbon Dioxide Adsorption Studies on Delafossite $CuFeO_2$ Hydrothermally Synthesized. *J. Phys. Chem. Solids* 2016, 98, 271−279.

(67) Barnabé, A.; Chapelle, A.; Presmanes, L.; Tailhades, P. Copper and iron based thin film nanocomposites prepared by radio frequency sputtering. Part I: elaboration and characterization of metal/oxide thin film nanocomposites using controlled in-situ reduction process. *J. Mater. Sci.* 2013, 48 (9), 3386−3394.

(68) Mugnier, E.; Barnabé, A.; Presmanes, L.; Tailhades, P. Thin film preparation by rf-sputtering of copper/iron ceramic targets with Cu/Fe = 1: from nanocomposites to delafossite compounds. *Thin Solid Films* 2008, 516 (7), 1453−1456.

(69) Barnabé, A.; Mugnier, E.; Presmanes, L.; Tailhades, P. Preparation of delafossite $CuFeO_2$ thin films by rf-sputtering on conventional glass substrate. *Mater. Lett.* 2006, 60 (29−30), 3468−3470.

(70) Lalanne, M.; Demont, P.; Barnabé, A. AC conductivity and dielectrics properties of $CuFe_{1-x}Cr_xO_2$:Mg delafossite. *J. Phys. D: Appl. Phys.* 2011, 44, 185401−185407.

(71) Spencer, P. Thermodynamic prediction of metastable coating structures in PVD processes. *Z. Metallkd.* **2001**, *92*, 1145−1150.

(72) Chang, K.; Music, D.; to Baben, M.; Lange, D.; Bolvardi, H.; Schneider, J. M. Modeling of metastable phase formation diagrams for sputtered thin films. *Sci. Technol. Adv. Mater.* **2016**, *17* (1), 210−219.

(73) Rodríguez-Carvajal, J. Recent Advances in Magnetic Structure Determination by Neutron Powder Diffraction. *Phys. B* **1993**, *192* (1−2), 55−69.

(74) Rietveld, H. M. A Profile Refinement Method for Nuclear and Magnetic Structures. *J. Appl. Crystallogr.* **1969**, *2* (2), 65−71.

(75) Gravereau, P. *Introduction à la pratique de la diffraction des rayons X par les poudres*, 3rd ed.; Université Bordeaux 1: Bordeaux , France, 2011; p 209.

(76) Brindley, G. W. The Effect of Grain or Particle Size on x-Ray Reflections from Mixed Powders and Alloys, Considered in Relation to the Quantitative Determination of Crystalline Substances by x-Ray Methods. *London, Edinburgh, Dublin Philos. Mag. J. Sci.* **1945**, *36* (256), 347−369.

(77) Wolff, N.; Klimm, D.; Siche, D. Thermodynamic Investigations on the Growth of $CuAlO_2$ Delafossite Crystals. *J. Solid State Chem.* **2018**, *258*, 495−500.

(78) Hellstén, N.; Hamuyuni, J.; Taskinen, P. High-Temperature Phase Equilibria of $Cu-O-Al_2O_3$ System in Air. *Can. Metall. Q.* **2016**, *55* (2), 226−233.

(79) de la Rubia, M. A.; Reinosa, J. J.; Leret, P.; Romero, J. J.; de Frutos, J.; Fernández, J. F. Experimental Determination of the Eutectic Temperature in Air of the $CuO-TiO_2$ Pseudobinary System. *J. Eur. Ceram. Soc.* **2012**, *32* (1), 71−76.

Supporting information

for

Insights on stability and cationic non-stoichiometry of CuFeO$_2$ delafossite

Juliano Schorne-Pinto[†‡], Laurent Cassayre[†], Lionel Presmanes[‡], Antoine Barnabé[‡]

† Laboratoire de Génie Chimique, Université de Toulouse, CNRS, Toulouse, France.

‡ CIRIMAT, Université de Toulouse, CNRS, Université Paul Sabatier, 118 Route de Narbonne, 31062 Toulouse Cedex 9, France.
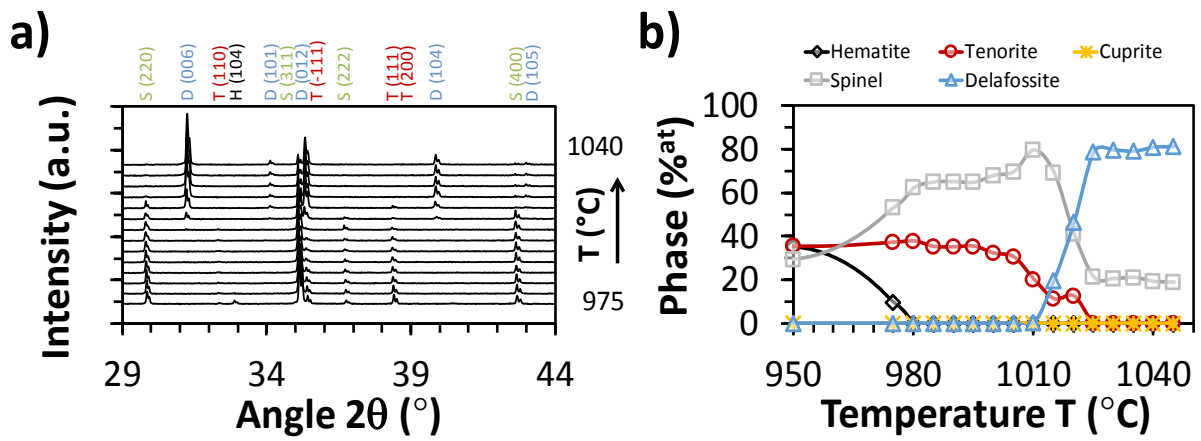
Figure S1: a) X-ray diffraction patterns for the sample x=0.52 over the temperature range 975-1045 °C from simple oxides. b) Corresponding amount of crystalline phases quantified by Rietveld refinement.